

# Comparison of Experimental and Simulated Turbulent Flow Around a Wing

---

Aytahn Ben-avi, Diogo Filipe Cravo da Costa, Tom van Aaken, Trey Gower

April 7, 2025

## CONTENTS

<b>1</b>	<b>Introduction</b>	<b>3</b>
<b>2</b>	<b>Definitions and Equations</b>	<b>3</b>
2.1	Reynolds Average Navier Stokes and Spalart-Allmaras . . . . .	3
2.2	Flow Comparison . . . . .	4
<b>3</b>	<b>Simulations</b>	<b>5</b>
3.1	Flow visualizations . . . . .	5
3.2	simpleFoam convergence . . . . .	10
<b>4</b>	<b>Comparison of Force Coefficients</b>	<b>13</b>
4.1	Force coefficients across angles of attack . . . . .	13
4.2	Moment coefficients across angles of attack . . . . .	15
4.3	Dependence on Reynolds number . . . . .	18
<b>5</b>	<b>Conclusion</b>	<b>21</b>
<b>6</b>	<b>Appendix</b>	<b>23</b>

# 1 INTRODUCTION

This exercise represents the confluence of previous work in COE 379L. Potential flow solutions around a 3D wing have already been presented, as well as Reynolds Averaged Navier Stokes (RANS) simulations around the simpler 'greenhouse' geometry. In this exercise, RANS simulations are carried out on the more complex 3D wing geometry. Force coefficients ( $C_{F_x}$ ,  $C_{F_y}$ ,  $C_{F_z}$ ) and the moment coefficients ( $C_{M_x}$ ,  $C_{M_y}$ ,  $C_{M_z}$ ) from the simulations are compared to those calculated for the wind tunnel data taken on the 3D wing earlier in the year. Flow visualizations are presented and simulation quality is assessed as well. The aim of this report is to conclude to some degree of certainty how well RANS simulations can approximate the real-world flow around a complex geometry, as well as any limitations that might bound its use in practice.

## 2 DEFINITIONS AND EQUATIONS

### 2.1 REYNOLDS AVERAGE NAVIER STOKES AND SPALART-ALLMARAS

The RANS equations are a widely used model for turbulent flows. The crux of RANS is the decomposition of a flow field, such as velocity or pressure, into a mean term and a fluctuation term. The mean term reflects the average condition of the flow over time. For flows that are considered statistically stationary, the mean term does not change with time. The fluctuation term reflects the elements of the flow that do change with time. In a turbulent flow situation, the fluctuation term would encompass the swirling eddies and vortices. The RANS decomposition for the velocity field is shown below:

$$\mathbf{u}(\mathbf{x}, t) = \bar{\mathbf{u}}(\mathbf{x}) + \mathbf{u}'(\mathbf{x}, t) \quad (2.1)$$

where  $\bar{\mathbf{u}}(\mathbf{x})$  is the mean term and  $\mathbf{u}'(\mathbf{x}, t)$  is the fluctuation term.

Expanding the RANS decomposition into the momentum equation yields the following:

$$\rho \bar{u}_j \frac{\partial \bar{u}_i}{\partial x_j} = \rho \bar{f}_i + \frac{\partial}{\partial x_j} \left[ -\bar{p} \delta_{ij} + \mu \left( \frac{\partial \bar{u}_i}{\partial x_j} + \frac{\partial \bar{u}_j}{\partial x_i} \right) - \rho \overline{u'_i u'_j} \right] \quad (2.2)$$

The Reynolds stress term  $-\rho \overline{u'_i u'_j}$  reflects the contributions of the fluctuation term. Between the momentum and continuity equations, there are not enough equations to solve for the Reynolds stress term, so a closure is needed. There are many different closures for the RANS model, each of which being more or less useful for particular flow situations. For this exercise, the Spalart-Allmaras closure is used. Spalart-Allmaras is known as an 'eddy viscosity closure' because it features a quantity called eddy viscosity. This quantity is introduced in the following equation:

$$-\overline{v'_i v'_j} = \nu_t \left( \frac{\partial \bar{v}_i}{\partial x_j} + \frac{\partial \bar{v}_j}{\partial x_i} \right) \quad (2.3)$$

Where  $\nu_t$  is the eddy viscosity. In order for this equation to act as a closure, no new variables can be introduced. In other words, the eddy viscosity needs to be calculated in some way from the mean fields described in the momentum and continuity equations. The Spalart-Allmaras closure is considered a 'one-equation model', because the eddy viscosity term is defined by the following single equation:

$$\frac{\partial \tilde{v}}{\partial t} + u_j \frac{\partial \tilde{v}}{\partial x_j} = C_{b1} [1 - f_{t2}] \tilde{S} \tilde{v} + \frac{1}{\sigma} \{ \nabla \cdot [(\nu + \tilde{v}) \nabla \tilde{v}] + C_{b2} |\nabla \tilde{v}|^2 \} - \left[ C_{w1} f_w - \frac{C_{b1}}{\kappa^2} f_{t2} \right] \left( \frac{\tilde{v}}{d} \right)^2 \quad (2.4)$$

Where  $\nu_t$  is calculated from the quantity  $\tilde{v}$ .

This set of equations is implemented in the OpenFOAM solver SimpleFoam in order to solve for the velocity and pressure fields over the desired computational domain.

## 2.2 FLOW COMPARISON

Relevant quantities for comparing the simulations and wind tunnel data are presented here.

Flow equivalency is established using the nondimensional quantity Reynolds number:

$$Re = \frac{u_\infty l}{\nu}. \quad (2.5)$$

Where  $u_\infty$  is the freestream fluid velocity,  $\nu$  is the kinematic viscosity, and  $l$  is a characteristic length. This characteristic length was chosen to be the root chord of the wing.

In order to define the force and moment coefficients, the dynamic pressure must first be defined:

$$q = \frac{1}{2} \rho u^2. \quad (2.6)$$

Where  $\rho$  is the density of the fluid, and  $u$  is the local velocity of the fluid. Now, the force coefficient in any of the three basis directions is defined as

$$C_i = \frac{F_i}{q_\infty S}. \quad (2.7)$$

Where  $F_i$  is the relevant force component,  $q_\infty$  is the freestream dynamic pressure, and  $S$  is a reference area. This reference area was chosen as the planform area of the wing. This area was calculated using CAD software, and double checked with elementary geometry.

The equations for moments of the wind tunnel data must be adjusted to reflect how OpenFOAM calculates the moments. In OpenFOAM, the moments are calculated at the quarter-chord point of the root section of the wing. In the wind tunnel, the sensor at which the moments are measured is offset by 0.0115 meters in the negative z-direction from the center of the mounting plate. Additionally, the wing is mounted to the center of the plate at 0.042075 meters in the positive x-direction and 0.00127 meters in the negative y-direction from the

quarter-chord point. The following equations are used to apply the requisite translations to the moments measured by the force balance:

$$M'_x = M_x - (-0.0115)F_y + (-0.00127)F_z \quad (2.8)$$

$$M'_y = M_y + (-0.0115)F_x - (0.042075)F_z \quad (2.9)$$

$$M'_z = M_z - (0.042075)F_y + (-0.00127)F_x \quad (2.10)$$

Now that the moment from the simulations and wind tunnel are defined around the same point (quarter-chord), the moment coefficients can now be defined as follows:

$$C_{M_i} = \frac{M_i}{q_\infty Sl}. \quad (2.11)$$

### 3 SIMULATIONS

This section contains some flow visualizations from a selection of simulations, as well as convergence plots to assess simulation quality. The following chart contains the full matrix of simulations that were run:

Re = 266000, $\alpha = -2.5^\circ$	Re = 189500, $\alpha = -2.5^\circ$	Re = 135500, $\alpha = -2.5^\circ$
Re = 266000, $\alpha = 0^\circ$	Re = 189500, $\alpha = 0^\circ$	Re = 135500, $\alpha = 0^\circ$
Re = 267000, $\alpha = 2.5^\circ$	Re = 190500, $\alpha = 2.5^\circ$	Re = 135600, $\alpha = 2.5^\circ$
Re = 267000, $\alpha = 5^\circ$	Re = 189800, $\alpha = 5^\circ$	Re = 134900, $\alpha = 5^\circ$
Re = 267000, $\alpha = 10^\circ$	Re = 189600, $\alpha = 10^\circ$	Re = 135500, $\alpha = 10^\circ$
Re = 267000, $\alpha = 12.5^\circ$	Re = 189500, $\alpha = 12.5^\circ$	Re = 135400, $\alpha = 12.5^\circ$

Table 3.1: Simulation Matrix for OpenFOAM Runs

All simulations are based on "3d-wing-RAS-Spalart-Allmaras-finemesh" found in the class repository. The only changes made to the files were to change the input Re and  $\alpha$ , as well as changing the allocation and decomposition to match the nodes and queues used on Frontera. The all final meshes with layers added contain approximately 22 million cells. Every simulation was run on 4 nodes with 56 cores, for a total of 224 cores. Each simulation took approximately 0.911 clock hours to run, which corresponds to 204.089 CPU hours.

#### 3.1 FLOW VISUALIZATIONS

Due to time and space constraints, flow visualizations and analysis cannot be presented for every simulation. However, what follows is a representative sample. These graphics were produced using the data from the last iteration of simpleFoam for the case with Re = 226000 and  $\alpha = 5^\circ$  and  $\alpha = 12.5^\circ$ .

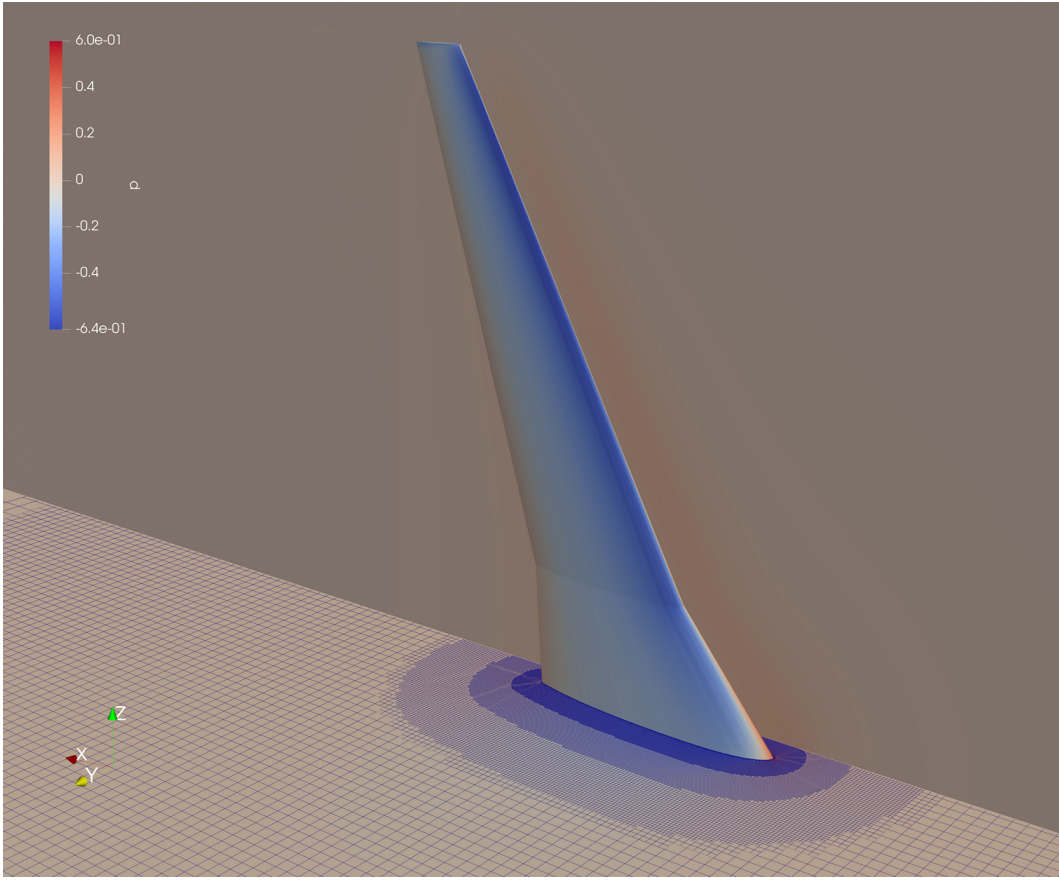


Figure 3.1: Pressure field and mesh at  $\text{Re} = 267000$ ,  $\alpha = 5^\circ$ , positive-Y side

In Figure 3.1 and Figure 3.2, multiple elements of the simulation workflow can be observed. On the bottom wall of the computational domain, the boundaries of cells are marked in blue. Here it is possible to see the areas where cells are gradually refined to be able to capture the more complex flow phenomena close to the wing. These refinement areas envelop the entirety of the wing, and are contained themselves within three further spherical regions of refinement that are not distinguishable in these images. Furthermore, the pressure acting on the wing and two surfaces around it is shown: it can be observed in Figure 3.1 that the region of the upper surface close to the leading edge experiences the highest drop in pressure. This is where the flow would be expected to accelerate around the curvature of the airfoil shape, so it is expected that the pressure be so low. Conversely, in Figure 3.2, the lower surface close to the leading edge shows a buildup of pressure where the stagnation point is expected to be. Also, the plane behind the wing is close enough to the latter's upper surface that the lower pressure zone is still visible in blue.

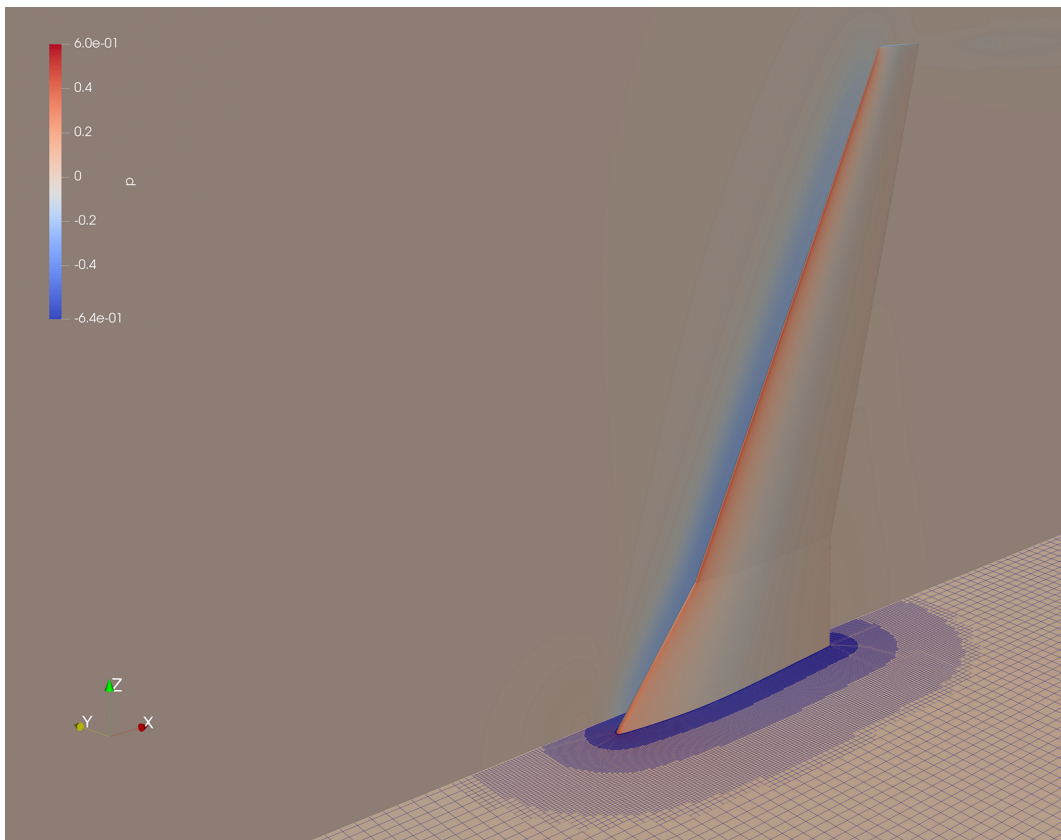


Figure 3.2: Pressure field and mesh at  $\text{Re} = 267000$ ,  $\alpha = 5^\circ$ , negative-Y side

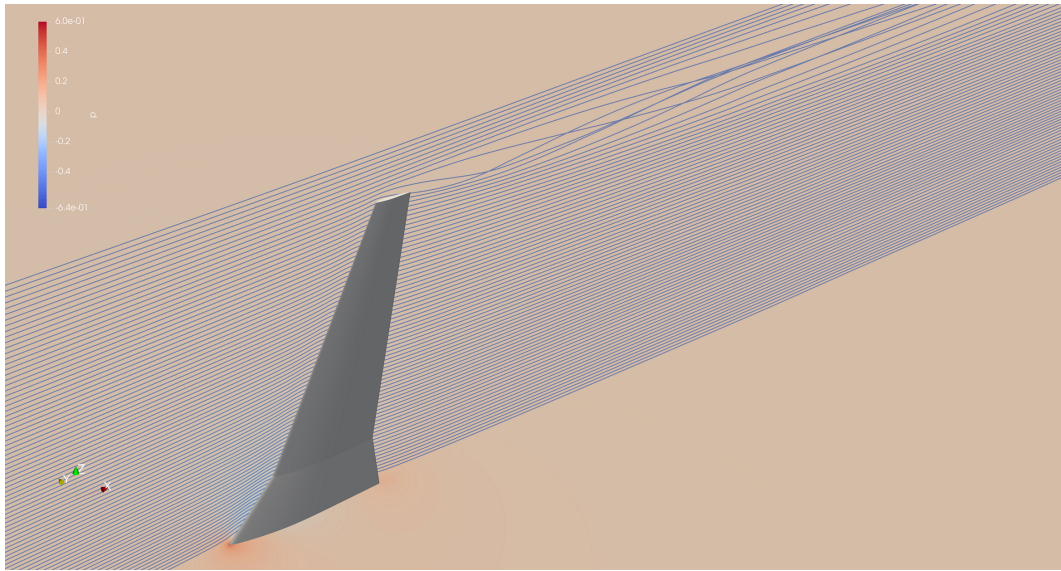


Figure 3.3: Pressure field and streamlines at  $\text{Re} = 267000$ ,  $\alpha = 5^\circ$ , negative-Y side

Figure 3.3 and 3.4 attempt to show the aerodynamic behavior of the air as it flows over the wing and around the wingtip. In the former it can be observed that when the angle of attack is low, the flow over the wing remains mostly unperturbed. The effects of separation, although not accurately simulable using the simpleFoam solver, are not expected to be appear at angles of attack as low as  $5^\circ$ . However, the effect of the pressure difference between the regions below and above the wing can be seen at the wingtip: here, these two separate flows recombine to produce tip vortices, which can easily be seen in both images.

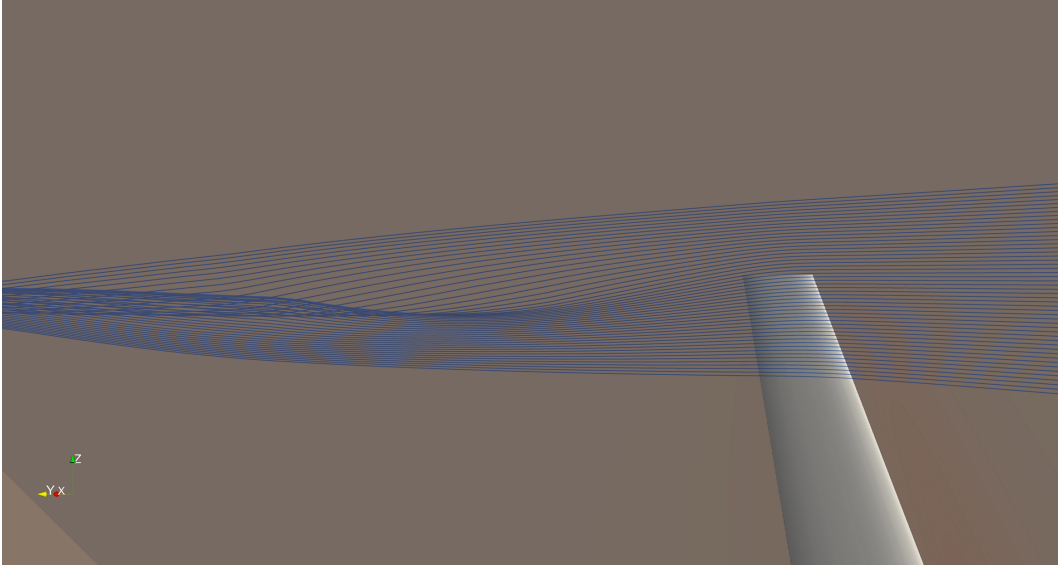


Figure 3.4: Tip vortex detail at  $Re = 267000$ ,  $\alpha = 5^\circ$

These flow visualizations do not yield anything particularly unexpected. There is lower pressure on the positive-Y side of the airfoil and higher pressure on the negative-Y side, as one would expect at a positive angle of attack. That pressure differential is characteristic of lift generation. In the images with streamlines, it appears as though some vorticity is generated at the wingtips, which is also expected. The flow appears to remain attached across the full span of the wing, which should be the case at this moderate angle of attack.

However, as the angle start increasing, the behavior of the flow changes drastically. While the pressure remains generally low on the positive-Y side and high on the negative-Y side, the pressure field overall is much less uniform, especially towards the wingtip. This can be seen clearly in Figure 3.5. This indicates that flow separation may be occurring towards the wingtip, otherwise known as tip stall. The additional turbulence at this higher angle of attack is also reflected in the streamlines. In addition to the wingtip vortex also seen at the lower angle of attack, there is vorticity along roughly the outer half of the trailing edge, visible in Figure 3.6. Once again, this is not unexpected given this more extreme angle of attack. However, the accuracy of the flow state in these conditions is also more questionable than for those at lower angles of attack, since the underlying equations that make up the simpleFoam solver are not well-suited to predicting and simulating full separation and its effects.

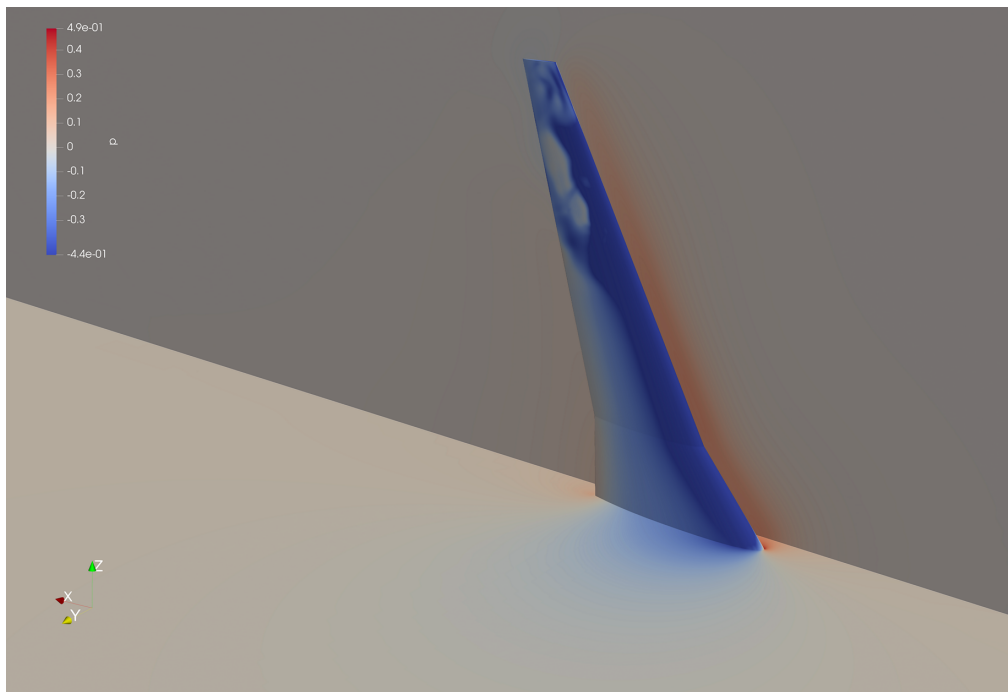


Figure 3.5: Pressure field at  $Re = 267000$ ,  $\alpha = 12.5^\circ$ , positive-Y side

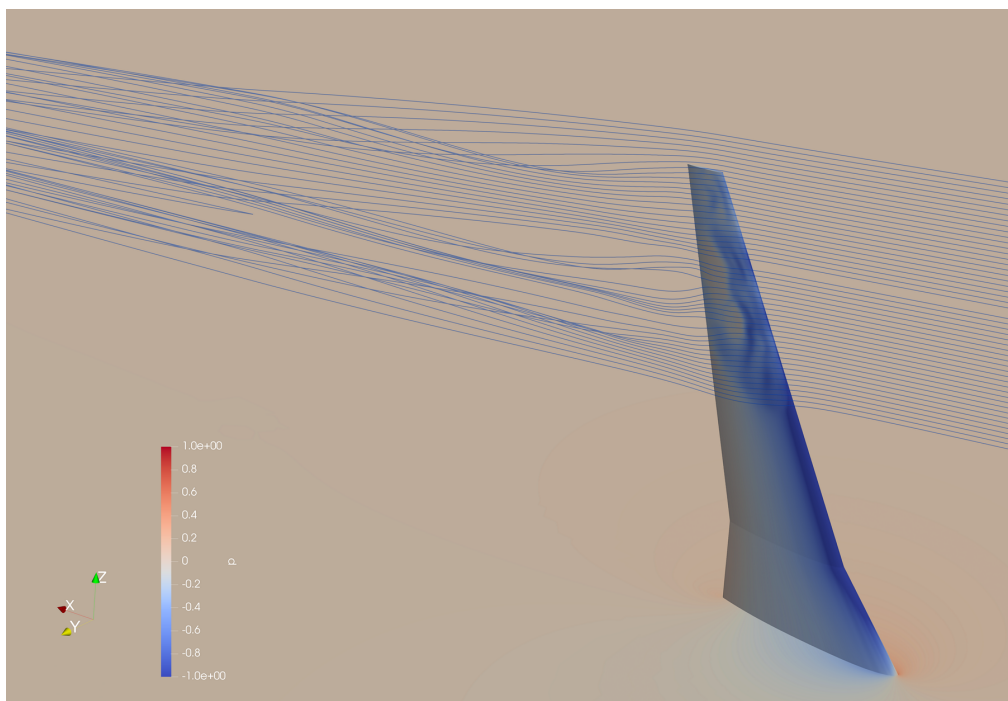


Figure 3.6: Pressure field with streamlines at  $Re = 267000$ ,  $\alpha = 12.5^\circ$ , positive-Y side

### 3.2 SIMPLEFOAM CONVERGENCE

The simpleFoam solver was set to run for a maximum of 2000 iterations after testing different limits. It was found that 2000 was the optimal point for convergence of all simulations in the test matrix, even those with more challenging conditions for convergence to occur in, while not being unnecessarily expensive in terms of CPU-hours. It was found to be more computationally- and time efficient to use a quick preliminary potentialFoam solution as an initial guess for simpleFoam to start its iterative process from, instead of first running simpleFoam on a coarser mesh.

Figure 3.7, 3.8, 3.9 and 3.10 show some example of how the residuals of different simulation parameters progressed over the 200 timesteps in different simulation conditions.

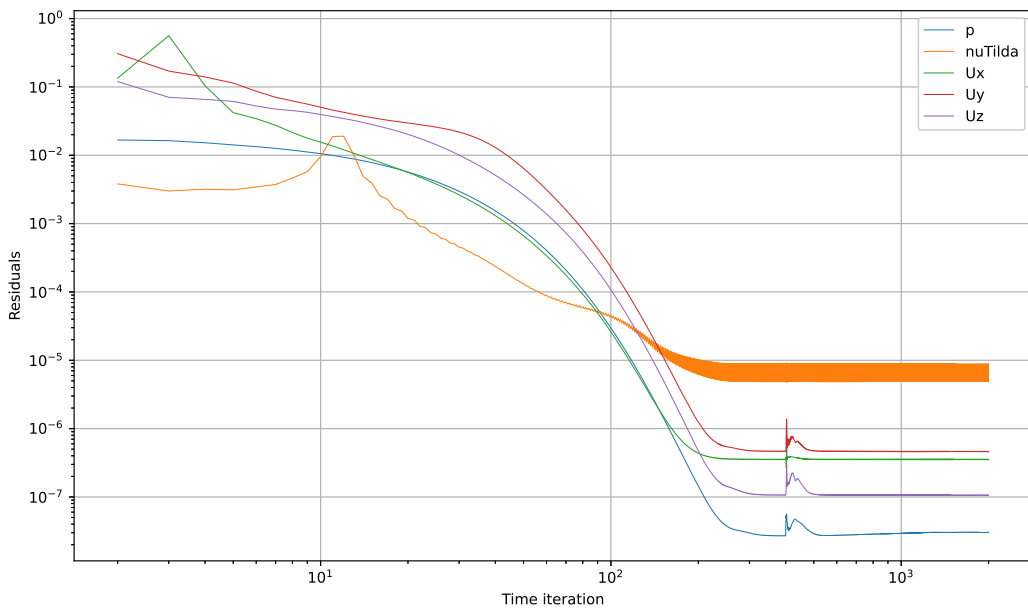


Figure 3.7: Residuals for  $Re = 266000, \alpha = 0$

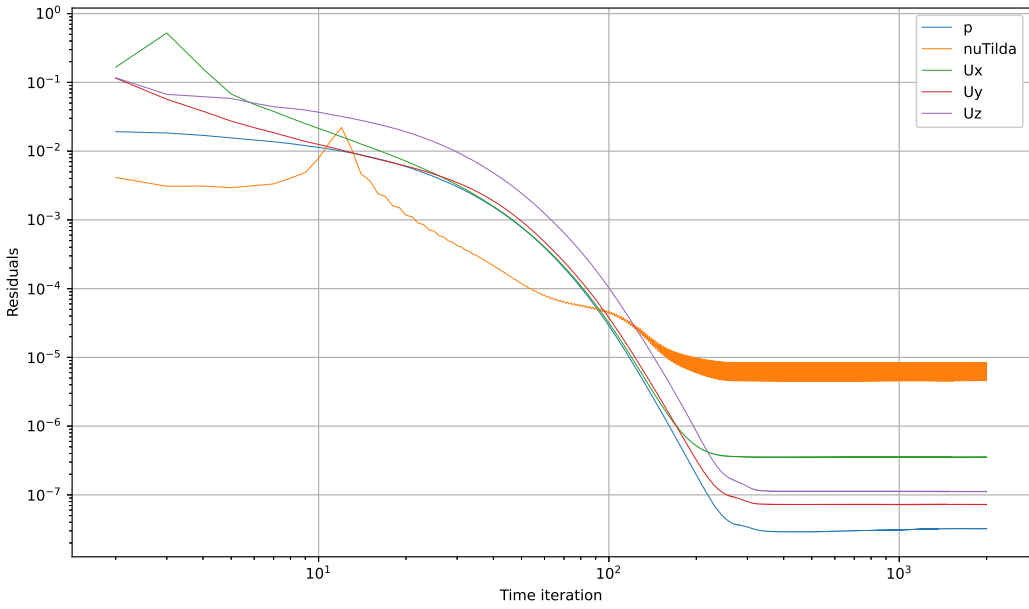


Figure 3.8: Residuals for  $Re = 267000$ ,  $\alpha = 2.5$

At lower angles of attack, like  $0^\circ$  and  $2.5^\circ$  shown above, simpleFoam easily converges within 2000 iterations. Across The highest residuals are those of the  $\tilde{v}$  field, and the lowest are those of the pressure field.

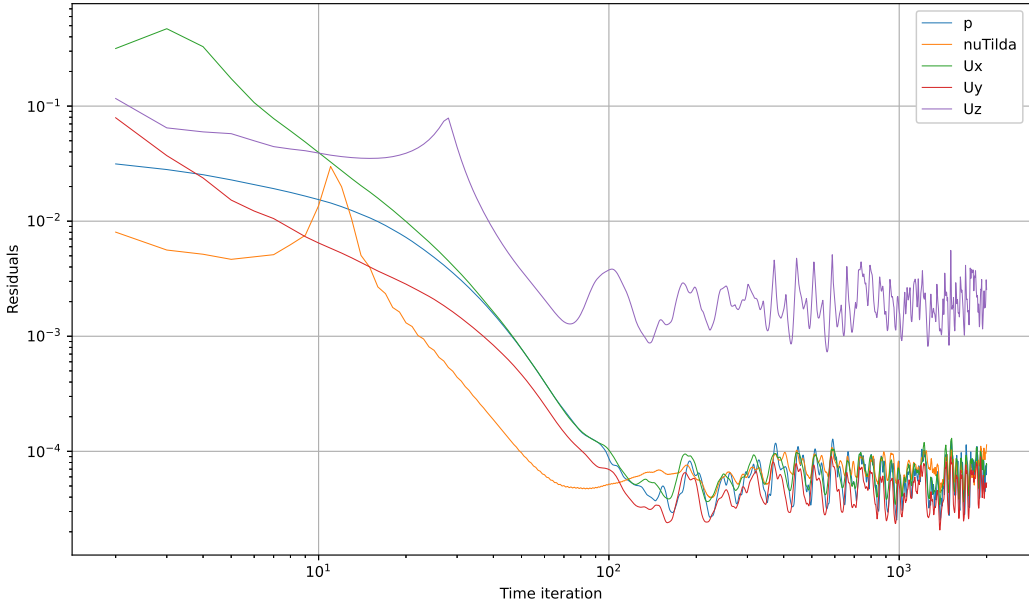


Figure 3.9: Residuals for  $Re = 266000$ ,  $\alpha = 10$

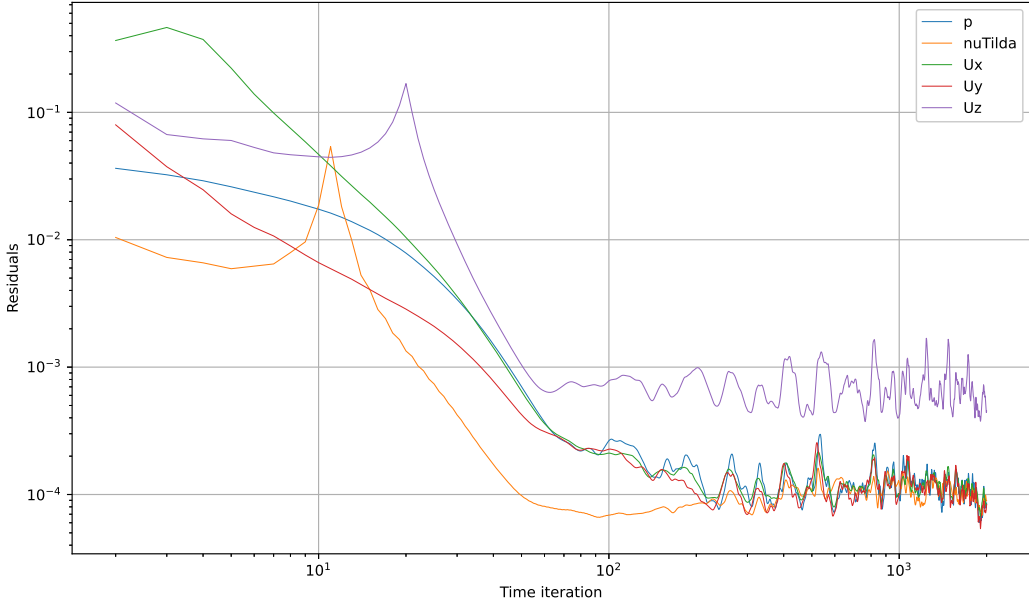


Figure 3.10: Residuals for  $Re = 267000$ ,  $\alpha = 12.5$

At higher angles of attack, like  $10^\circ$  and  $12.5^\circ$  shown above, simpleFoam has a little bit more trouble. Although the residuals do end up being very small, they are oscillating at the final timestep. This would indicate that although the error is small, strictly speaking the solution has not converged, because it is still changing (albeit very slightly). Convergence at high angles of attack is more difficult to achieve because of the additional fluctuations in the flow. It is also possible that mesh quality has suffered a little bit due to the 'twist' in the mesh that occurs when an angle of attack is applied. Interestingly, the residual of greatest magnitude is now the  $U_z$  field.

## 4 COMPARISON OF FORCE COEFFICIENTS

In this section the most important results from both types of data collection are presented and compared. The metrics being used are the non-dimensional force and moment coefficients, calculated as described above and in previous reports.

### 4.1 FORCE COEFFICIENTS ACROSS ANGLES OF ATTACK

First, the relationships between the three force coefficients and the angle of attack are considered.

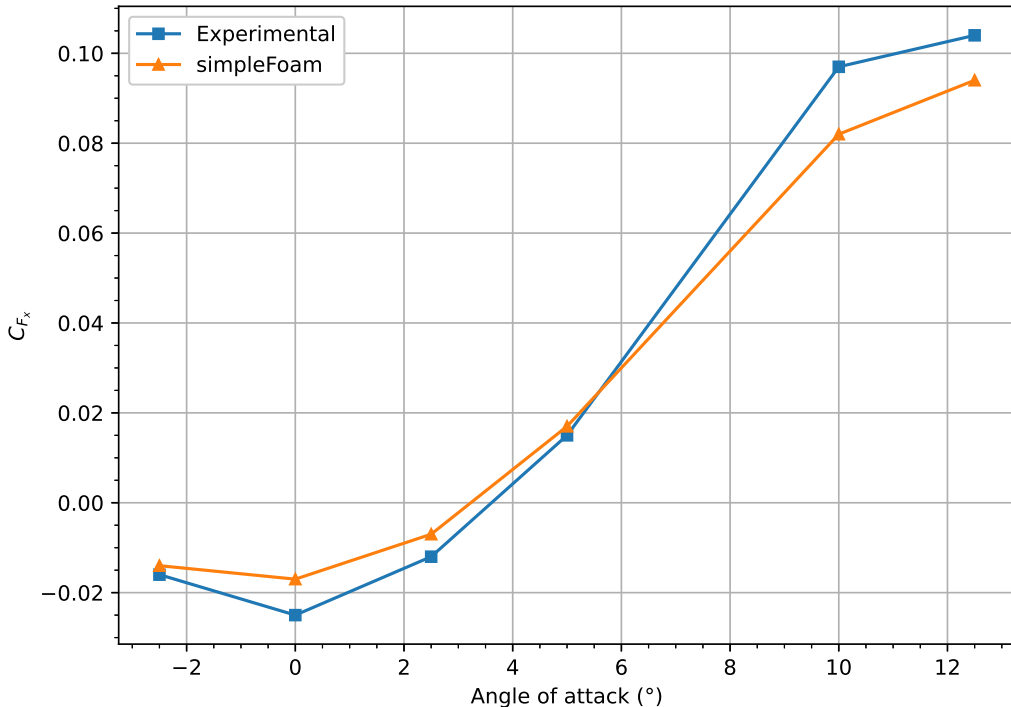


Figure 4.1: Plot of  $C_{F_x}$  against  $\alpha$ ,  $Re = 266000-267000$

The agreement between simulations and experiments is significant. Additionally, the values behave as one would expect based on the physics of the flow condition. In the coordinate system of these experiments,  $C_{F_x}$  corresponds to the drag coefficient of the wing. One would therefore expect to see the lowest drag coefficient at  $\alpha = 0^\circ$ , and see increasing drag coefficients as  $\alpha$  increases both in the negative and positive directions. This is reflected in both the simulated and experimental data, which share a qualitative similarity in that the shapes of the two curves are much alike.

One interesting point to note is that the drag force was recorded to be negative at and around  $0^\circ$  both in the wind tunnel experiments and simulations. This would imply a sort of thrust force is generated, which would appear to be a dubious a physical scenario. The experimental

value could be explained as an error coming from the data collection process. The true value of the force is so small that the precision setting of the force balance required to resolve the larger forces such as lift may have inhibited its ability to determine smaller forces like drag with accuracy. However, the fact that also the simulations reflect the same relationship may suggest some other secondary phenomena affecting the forces exists.

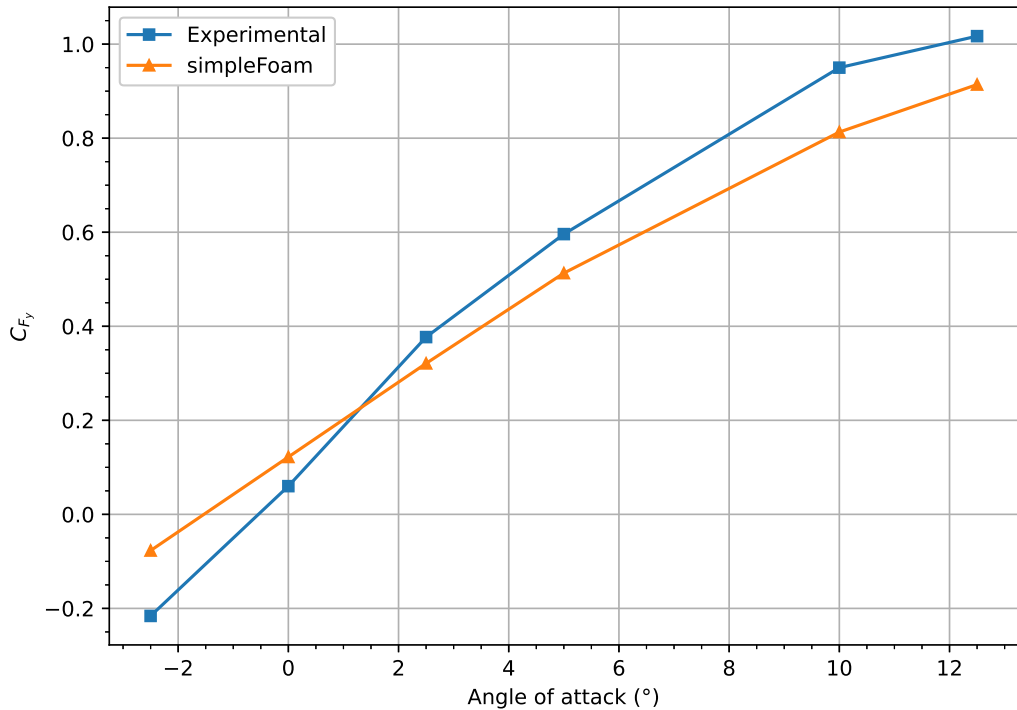


Figure 4.2: Plot of  $C_{F_y}$  against  $\alpha$ ,  $Re = 266000-267000$

Once again, the agreement between simulations and experiments here is very good: the values also still behave as one would expect based on the physics of the flow condition. Here,  $C_{F_y}$  corresponds to the lift coefficient of the wing, with a positive force being defined in the positive y-direction. One would therefore expect to see increasing lift coefficients as  $\alpha$  increases, up until the point where flow separation begins to take place. This is exactly what is seen in both datasets, with a fairly linear increase in  $C_{F_y}$  until it begins to taper off between  $\alpha = 10^\circ$  and  $\alpha = 12.5^\circ$ . From the flow visualizations above, it is known that flow separation is beginning to occur at these angles of attack, explaining smaller rate of increase in lift coefficient. However, full separation on large parts of the wing (stall) has not yet occurred at this point: were the tests to be expanded to include higher angles of attack, it would be expected that the difference in the two datasets would become much more significant towards those higher angles where simpleFoam is unable to accurately simulate the complex flow phenomena involved in a stall.

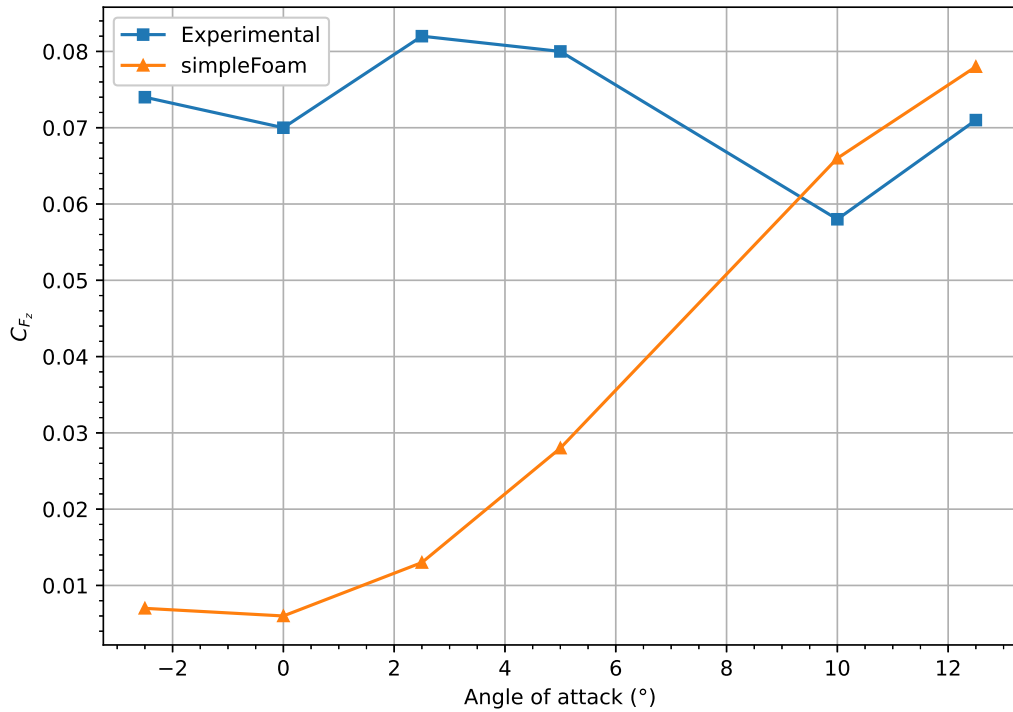


Figure 4.3: Plot of  $C_{F_z}$  against  $\alpha$ ,  $Re = 266000-267000$

$C_{F_z}$  is the spanwise force coefficient, associated with neither lift nor drag. Because the flow in the wind tunnel is in the chordwise direction, the values of  $F_z$ , and thus its coefficients, are quite small. As such, the error in both the simulations and the wind tunnel force balance setup become more apparent. It is also more difficult to assess what these data should look like based on experiments in the literature, as the spanwise forces are not as widely studied as lift and drag. While Figure 4.3 appears to show a large discrepancy between the data from the simulations and wind tunnel, it is important to note that the scale being used on the force coefficient axis is significantly smaller than that being used in previous figures. These differences are therefore discarded as insignificant in assessing the overall fidelity of simpleFoam.

#### 4.2 MOMENT COEFFICIENTS ACROSS ANGLES OF ATTACK

Next, the moment coefficients in the three axial directions are displayed across the range of angles tested, both in the wind tunnel and using RANS simulations.

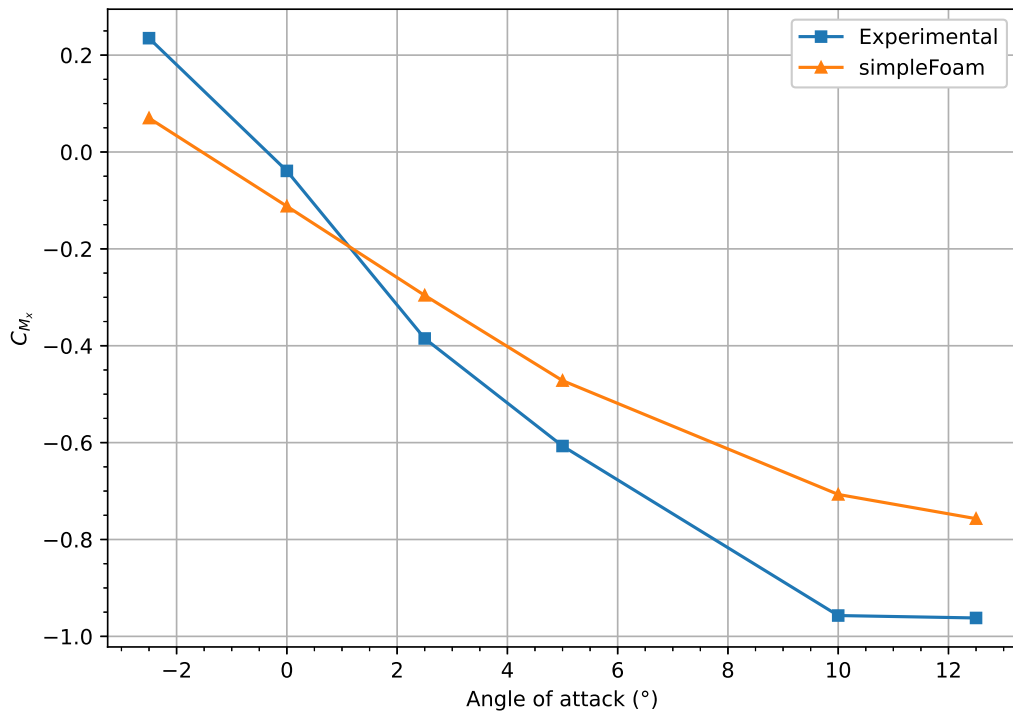


Figure 4.4: Plot of  $C_{M_x}$  against  $\alpha$ ,  $Re = 266000-267000$

Once again, agreement between simulations and experiments is good.  $C_{M_x}$  is mainly a function of  $F_y$  which corresponds to lift. Positive values of  $F_y$  applied at a positive-Z moment arm generate a negative x-direction moment, so it is expected that  $C_{M_x}$  decreases as the increasing angle of attack creates more lift. Just as the  $C_{F_y}$  began to taper off as flow separation begins occurring at high angles of attack, the decreases in  $C_{M_x}$  begin to slow as the same phenomenon occurs.

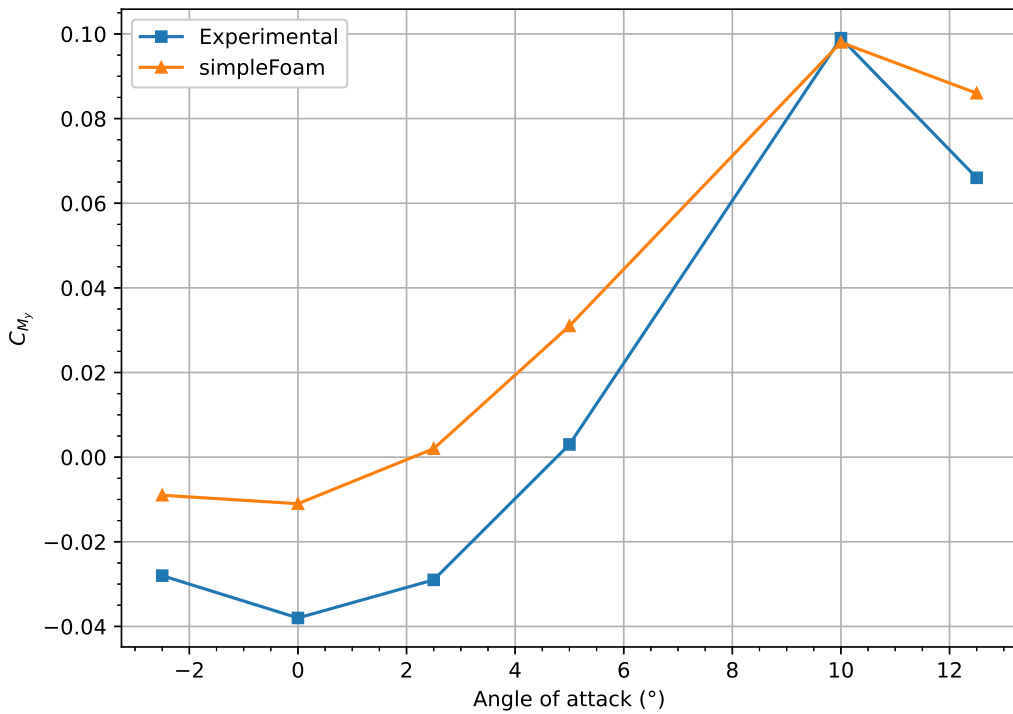


Figure 4.5: Plot of  $C_{M_y}$  against  $\alpha$ ,  $Re = 266000-267000$

Once again, agreement between simulations and experiments is good.  $C_{M_y}$  is mainly a function of  $F_x$  which corresponds to drag. Positive values of  $F_x$  applied at a positive-Z moment arm generate a positive y-direction moment, so it is expected that  $C_{M_y}$  increases as the increasing angle of attack creates more drag.

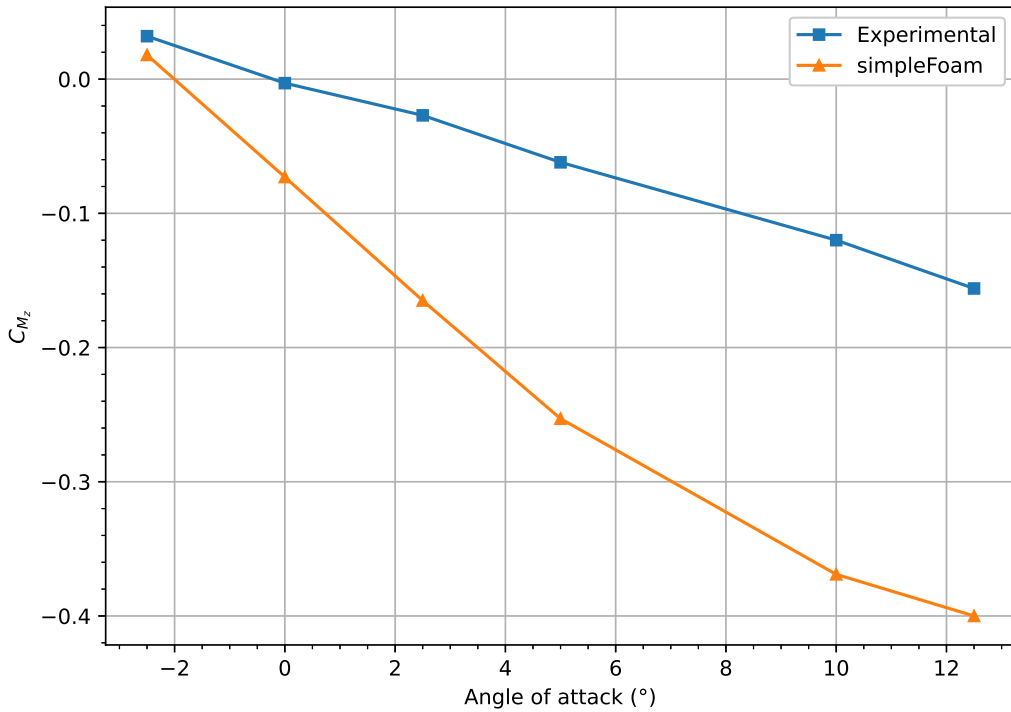


Figure 4.6: Plot of  $C_{M_z}$  against  $\alpha$ ,  $Re = 266000-267000$

In the coordinate system of these experiments,  $C_{M_z}$  corresponds to the pitching moment of the wing. As discussed earlier, simpleFoam's utilities calculate moments around the quarter-chord point, and the wind tunnel data have been adjusted to match. The quarter-chord point is significant in aerodynamics because for many airfoils it does not see any change in moment with respect to changing angle of attack. According to this plot, this is not the case for the wing tested in this project, as both the experimental data and simulation results show a decreasing value of  $C_{M_z}$  as angle of attack increases. Also notable is the fact that simpleFoam underpredicts the experimental value by some margin, something not seen in most of the other coefficient plots. The difference is particularly severe at higher angles of attack, which could be explained by the failure of high angle of attack simulations to completely converge within the allotted timesteps. However, the other coefficients do not see such a discrepancy at high angles of attack, so this explanation is not conclusive.

### 4.3 DEPENDENCE ON REYNOLDS NUMBER

In this final subsection, the two data collection methods are considered separately as the effects of varying Reynolds number on the force and moment coefficients are investigated.

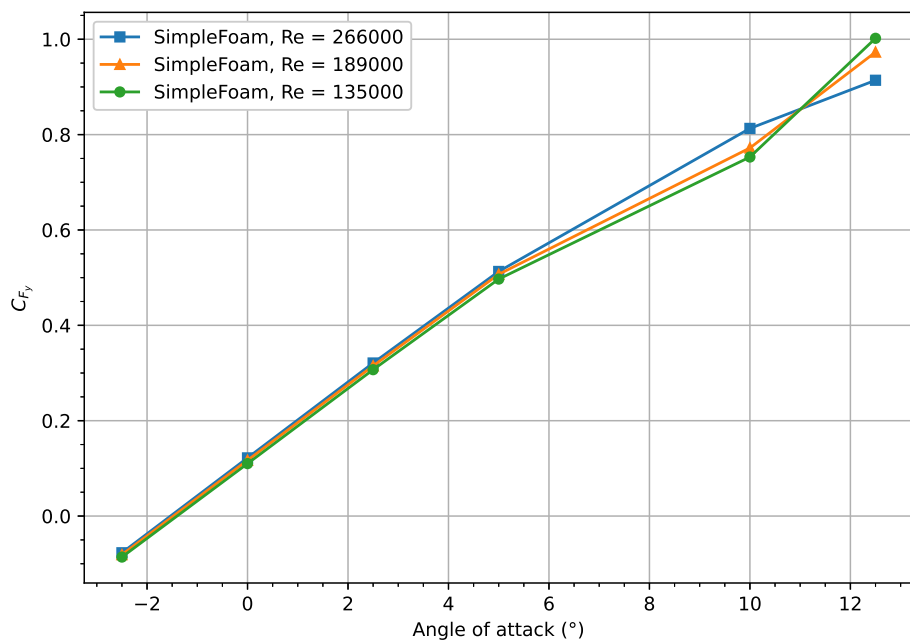
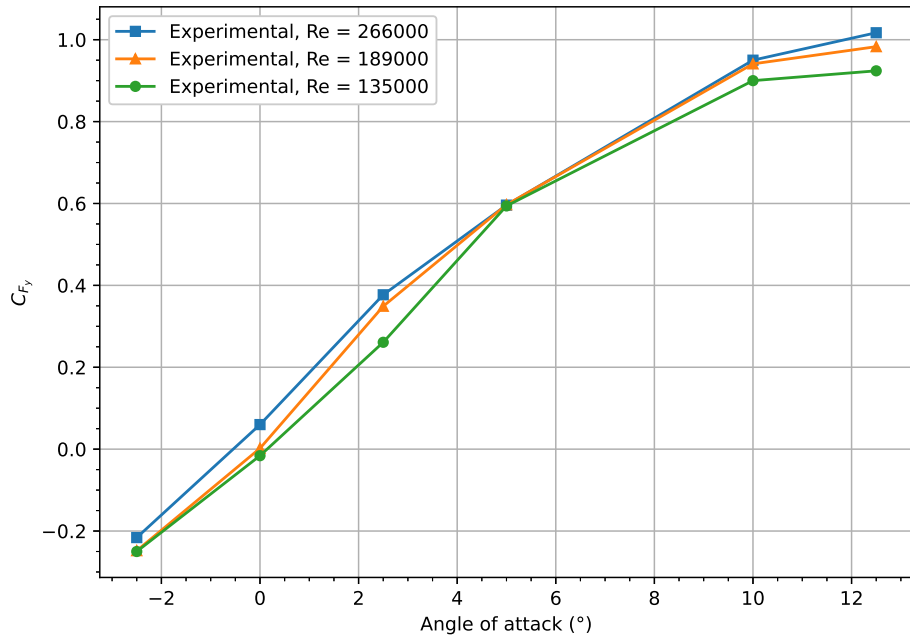


Figure 4.7 and Figure 4.8 above show the lift coefficient as a function of angle of attack for all three Reynolds numbers that were tested. The first plot illustrates this for the wind tunnel data, and the second for the simpleFoam simulations. In both cases, the pattern of a fairly linear increase in  $C_{F_y}$  with increasing  $\alpha$  is consistent across Reynolds numbers. In both cases, the highest Reynolds number tested yields the highest values of  $C_{F_y}$ , but only by a very slim margin. The lift coefficient barely changes with Reynolds number.

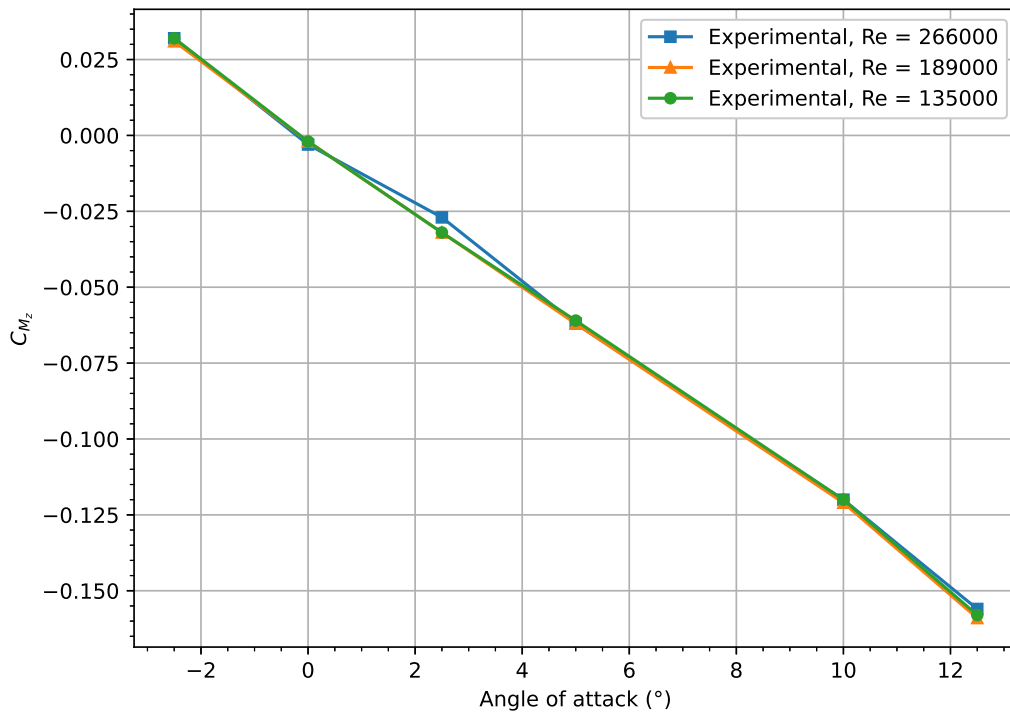


Figure 4.9: Plot of  $C_{M_z}$  against  $\alpha$ , Wind Tunnel data

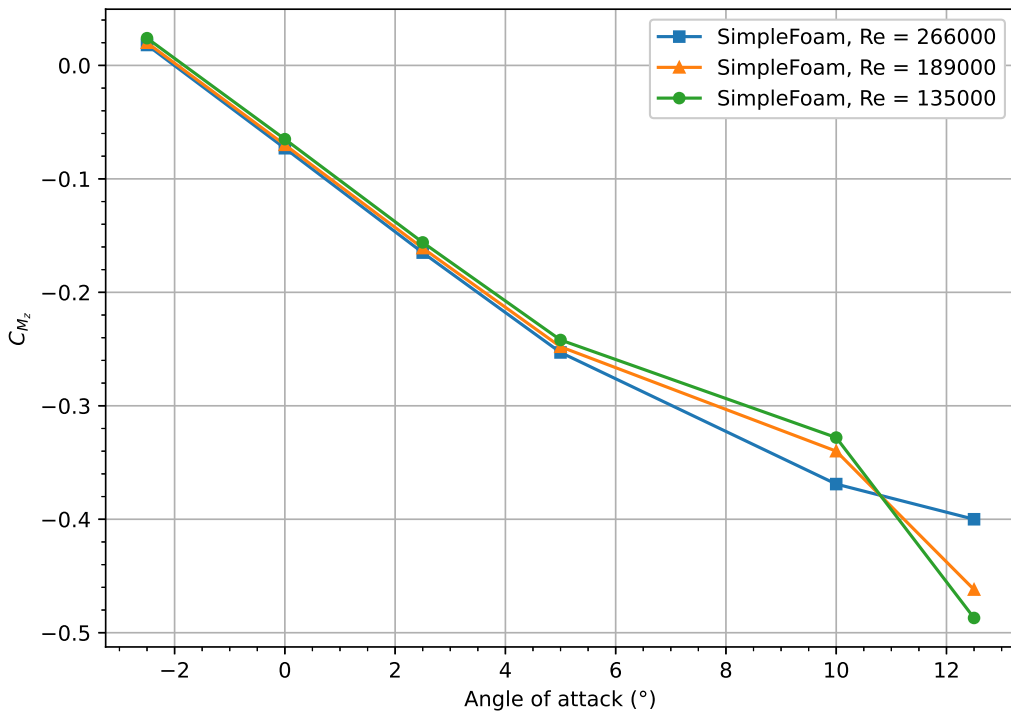


Figure 4.10: Plot of  $C_{M_z}$  against  $\alpha$ , simpleFoam data

Now looking instead at the moment coefficients, Figure 4.9 and Figure 4.10 above show the pitching moment coefficient as a function of angle of attack for all three Reynolds numbers that were tested. The first plot illustrates this for the wind tunnel data, and the second for the simpleFoam simulations. In both cases, the pattern of a fairly linear decrease in  $C_{M_z}$  with increasing  $\alpha$  is consistent across Reynolds numbers. In both cases, the difference between results for each Reynolds number is very slight. In the case of simpleFoam, the agreement starts to get a bit looser as angle of attack increases, which could be a result of the aforementioned convergence issues at higher angles of attack.

## 5 CONCLUSION

The aims of this exercise were to assess how well RANS simulations can approximate the real-world flow around a complex geometry, as well as to explore their limitations. Based on the results presented above, it is clear that RANS is fairly capable of predicting lower-to-medium Reynolds number flows of the sort studied here. Agreement between nearly all force and moment coefficients was very good. There are, however, some limitations to the capabilities of simpleFoam. Although it can model turbulence, it is unable to resolve situations of total flow separation. As such, determining the exact point at which a wing stalls would be difficult with this particular RANS solver. Additionally, it is unknown whether this method would be as effective at predicting flows of higher Reynolds numbers than the ones tested here.

Nevertheless, the benefits of using RANS are undeniable: overall, the computational costs are acceptably low. To run the 18 separate simulations required by the test matrix in this project, on the order of hundreds of CPU cores were used for tens of hours. Compared to more accurate methods such as direct numerical simulation of the full Navier-Stokes equations, it becomes clear that this scheme can be used to quickly and (relatively) cheaply assess the aerodynamic performance of an object. This makes RANS ideally suited to an iterative design process of objects immersed in low-to-medium Reynolds number flows where separation is not likely to occur.

## 6 APPENDIX

The complete set of force and moment coefficients calculated from the raw data collected both in the wind tunnel and through the RANS simulations is presented below in Table 6.1 to Table 6.6 for the readers' reference.

Table 6.1:  $C_{F_x}$  for each flow condition

<b>Flow Condition</b>	<b>Tunnel</b>	<b>RANS</b>
Re = 266000, $\alpha = -2.5^\circ$	-0.016	-0.014
Re = 266000, $\alpha = 0^\circ$	-0.025	-0.017
Re = 267000, $\alpha = 2.5^\circ$	-0.012	-0.007
Re = 267000, $\alpha = 5^\circ$	0.015	0.017
Re = 267000, $\alpha = 10^\circ$	0.097	0.082
Re = 267000, $\alpha = 12.5^\circ$	0.104	0.094
Re = 189500, $\alpha = -2.5^\circ$	-0.017	-0.015
Re = 189500, $\alpha = 0^\circ$	-0.028	-0.018
Re = 190500, $\alpha = 2.5^\circ$	-0.017	-0.008
Re = 189800, $\alpha = 5^\circ$	0.013	0.015
Re = 189600, $\alpha = 10^\circ$	0.088	0.065
Re = 189500, $\alpha = 12.5^\circ$	0.084	0.07
Re = 135500, $\alpha = -2.5^\circ$	-0.019	-0.017
Re = 135500, $\alpha = 0^\circ$	-0.030	-0.020
Re = 135600, $\alpha = 2.5^\circ$	-0.024	-0.010
Re = 134900, $\alpha = 5^\circ$	0.011	0.013
Re = 135500, $\alpha = 10^\circ$	0.075	0.061
Re = 135400, $\alpha = 12.5^\circ$	0.062	0.062

Table 6.2:  $C_{F_y}$  for each flow condition

<b>Flow Condition</b>	<b>Tunnel</b>	<b>RANS</b>
Re = 266000, $\alpha = -2.5^\circ$	-0.216	-0.077
Re = 266000, $\alpha = 0^\circ$	0.060	0.122
Re = 267000, $\alpha = 2.5^\circ$	0.377	0.321
Re = 267000, $\alpha = 5^\circ$	0.596	0.513
Re = 267000, $\alpha = 10^\circ$	0.950	0.813
Re = 267000, $\alpha = 12.5^\circ$	1.017	0.914
Re = 189500, $\alpha = -2.5^\circ$	-0.248	-0.081
Re = 189500, $\alpha = 0^\circ$	0.002	0.117
Re = 190500, $\alpha = 2.5^\circ$	0.349	0.315
Re = 189800, $\alpha = 5^\circ$	0.597	0.507
Re = 189600, $\alpha = 10^\circ$	0.941	0.772
Re = 189500, $\alpha = 12.5^\circ$	0.983	0.973
Re = 135500, $\alpha = -2.5^\circ$	-0.250	-0.086
Re = 135500, $\alpha = 0^\circ$	-0.016	0.110
Re = 135600, $\alpha = 2.5^\circ$	0.261	0.307
Re = 134900, $\alpha = 5^\circ$	0.594	0.497
Re = 135500, $\alpha = 10^\circ$	0.900	0.753
Re = 135400, $\alpha = 12.5^\circ$	0.924	1.002

Table 6.3:  $C_{F_z}$  for each flow condition

<b>Flow Condition</b>	<b>Tunnel</b>	<b>RANS</b>
Re = 266000, $\alpha = -2.5^\circ$	0.074	0.007
Re = 266000, $\alpha = 0^\circ$	0.070	0.006
Re = 267000, $\alpha = 2.5^\circ$	0.082	0.013
Re = 267000, $\alpha = 5^\circ$	0.080	0.028
Re = 267000, $\alpha = 10^\circ$	0.058	0.066
Re = 267000, $\alpha = 12.5^\circ$	0.071	0.078
Re = 189500, $\alpha = -2.5^\circ$	0.100	0.007
Re = 189500, $\alpha = 0^\circ$	0.099	0.006
Re = 190500, $\alpha = 2.5^\circ$	0.116	0.013
Re = 189800, $\alpha = 5^\circ$	0.110	0.027
Re = 189600, $\alpha = 10^\circ$	0.081	0.059
Re = 189500, $\alpha = 12.5^\circ$	0.106	0.068
Re = 135500, $\alpha = -2.5^\circ$	0.128	0.007
Re = 135500, $\alpha = 0^\circ$	0.127	0.006
Re = 135600, $\alpha = 2.5^\circ$	0.146	0.013
Re = 134900, $\alpha = 5^\circ$	0.140	0.026
Re = 135500, $\alpha = 10^\circ$	0.109	0.057
Re = 135400, $\alpha = 12.5^\circ$	0.142	0.065

Table 6.4:  $C_{M_x}$  for each flow condition

<b>Flow Condition</b>	<b>Tunnel</b>	<b>RANS</b>
Re = 266000, $\alpha = -2.5^\circ$	0.235	0.070
Re = 266000, $\alpha = 0^\circ$	-0.039	-0.112
Re = 267000, $\alpha = 2.5^\circ$	-0.385	-0.296
Re = 267000, $\alpha = 5^\circ$	-0.607	-0.472
Re = 267000, $\alpha = 10^\circ$	-0.957	-0.707
Re = 267000, $\alpha = 12.5^\circ$	-0.962	-0.757
Re = 189500, $\alpha = -2.5^\circ$	0.269	0.074
Re = 189500, $\alpha = 0^\circ$	0.013	-0.107
Re = 190500, $\alpha = 2.5^\circ$	-0.339	-0.29
Re = 189800, $\alpha = 5^\circ$	-0.609	-0.464
Re = 189600, $\alpha = 10^\circ$	-0.945	-0.64
Re = 189500, $\alpha = 12.5^\circ$	-0.907	-0.858
Re = 135500, $\alpha = -2.5^\circ$	0.256	0.080
Re = 135500, $\alpha = 0^\circ$	0.029	-0.100
Re = 135600, $\alpha = 2.5^\circ$	-0.240	-0.280
Re = 134900, $\alpha = 5^\circ$	-0.605	-0.454
Re = 135500, $\alpha = 10^\circ$	-0.892	-0.617
Re = 135400, $\alpha = 12.5^\circ$	-0.826	-0.894

Table 6.5:  $C_{M_y}$  for each flow condition

<b>Flow Condition</b>	<b>Tunnel</b>	<b>RANS</b>
Re = 266000, $\alpha = -2.5^\circ$	-0.028	-0.009
Re = 266000, $\alpha = 0^\circ$	-0.038	-0.011
Re = 267000, $\alpha = 2.5^\circ$	-0.029	0.002
Re = 267000, $\alpha = 5^\circ$	0.003	0.031
Re = 267000, $\alpha = 10^\circ$	0.099	0.098
Re = 267000, $\alpha = 12.5^\circ$	0.066	0.086
Re = 189500, $\alpha = -2.5^\circ$	-0.036	-0.01
Re = 189500, $\alpha = 0^\circ$	-0.048	-0.012
Re = 190500, $\alpha = 2.5^\circ$	-0.045	0.001
Re = 189800, $\alpha = 5^\circ$	-0.007	0.029
Re = 189600, $\alpha = 10^\circ$	0.077	0.066
Re = 189500, $\alpha = 12.5^\circ$	0.028	0.057
Re = 135500, $\alpha = -2.5^\circ$	-0.049	-0.011
Re = 135500, $\alpha = 0^\circ$	-0.059	-0.014
Re = 135600, $\alpha = 2.5^\circ$	-0.061	-0.001
Re = 134900, $\alpha = 5^\circ$	-0.021	0.027
Re = 135500, $\alpha = 10^\circ$	0.050	0.061
Re = 135400, $\alpha = 12.5^\circ$	-0.010	0.053

Table 6.6:  $C_{M_z}$  for each flow condition

<b>Flow Condition</b>	<b>Tunnel</b>	<b>RANS</b>
Re = 266000, $\alpha = -2.5^\circ$	0.032	-0.018
Re = 266000, $\alpha = 0^\circ$	-0.003	-0.073
Re = 267000, $\alpha = 2.5^\circ$	-0.027	-0.165
Re = 267000, $\alpha = 5^\circ$	-0.062	-0.253
Re = 267000, $\alpha = 10^\circ$	-0.120	-0.369
Re = 267000, $\alpha = 12.5^\circ$	-0.156	-0.400
Re = 189500, $\alpha = -2.5^\circ$	0.031	0.02
Re = 189500, $\alpha = 0^\circ$	-0.002	-0.07
Re = 190500, $\alpha = 2.5^\circ$	-0.032	-0.161
Re = 189800, $\alpha = 5^\circ$	-0.062	-0.248
Re = 189600, $\alpha = 10^\circ$	-0.121	-0.34
Re = 189500, $\alpha = 12.5^\circ$	-0.159	-0.462
Re = 135500, $\alpha = -2.5^\circ$	0.032	0.024
Re = 135500, $\alpha = 0^\circ$	-0.002	-0.065
Re = 135600, $\alpha = 2.5^\circ$	-0.032	-0.156
Re = 134900, $\alpha = 5^\circ$	-0.061	-0.242
Re = 135500, $\alpha = 10^\circ$	-0.120	-0.328
Re = 135400, $\alpha = 12.5^\circ$	-0.158	-0.487